PHOTONICS Research

Meta-objective with sub-micrometer resolution for microendoscopes

Yan Liu,[1,†] Qing-Yun Yu,[1,†] Ze-Ming Chen,[1,†] Hao-Yang Qiu,[1] Rui Chen,[1] Shao-Ji Jiang,[1] Xin-Tao He,[1,2] Fu-Li Zhao,[1,3] and Jian-Wen Dong[1,*]

[1]School of Physics & State Key Laboratory of Optoelectronic Materials and Technologies, Sun Yat-sen University, Guangzhou 510275, China
[2]e-mail: hext9@mail.sysu.edu.cn
[3]e-mail: stszfl@mail.sysu.edu.cn
*Corresponding author: dongjwen@mail.sysu.edu.cn

Received 24 August 2020; revised 29 November 2020; accepted 29 November 2020; posted 30 November 2020 (Doc. ID 406197); published 14 January 2021

Microendoscopes are vital for disease detection and clinical diagnosis. The essential issue for microendoscopes is to achieve minimally invasive and high-resolution observations of soft tissue structures inside deep body cavities. Obviously, the microscope objective is a must with the capabilities of both high lateral resolution in a wide field of view (FOV) and miniaturization in size. Here, we propose a meta-objective, i.e., microscope objective based on cascaded metalenses. The two metalenses, with the optical diameters of 400 μm and 180 μm, respectively, are mounted on both sides of a 500-μm-thick silica film. Sub-micrometer lateral resolution reaches as high as 775 nm in such a naked meta-objective, with monochromatic aberration correction in a 125 μm full FOV and near diffraction limit imaging. Combined with a fiber bundle microscope system, the single cell contour of biological tissue (e.g., water lily leaf) can be clearly observed, compared to the indistinguishable features in other conventional lens-based fiber bundle systems, such as plano–convex and gradient refractive index (GRIN) cases.

https://doi.org/10.1364/PRJ.406197

1. INTRODUCTION

Endoscopy, in the basic forms of modern endoscopy, was initiated by Dr. Philipp Bozzini in the early 19th century [1,2]. In recent years, the fiber bundle-based microendoscope [3,4] has become one of the most important tools for early cancer screening, composed of a miniature microscope objective and external instruments, such as confocal reflectance and fluorescence [5,6], multi- and two-photon [7–10], and structured illumination [11,12] systems. Due to the limitations of the diameter and spacing of the fiber cores in the fiber bundle, it is difficult to achieve single cell resolution. Therefore, the fiber bundle microendoscope is usually integrated with a miniature microscope objective in order to provide sufficient resolution to observe the cellular structure of tissue without any scanning equipment. It can deeply penetrate into the body cavity for histopathological diagnosis, including in lung cancer [13], gastric tumors [14], and colorectal cancer [15].

High resolution and miniaturization are two important issues of endoscopic imaging. The miniature microscope objective forms the first inverted intermediate image, playing a decisive role in the resolution of endoscopic imaging. In order to reduce the discomfort of patients and make conventional diagnosis and treatment more efficient, the size of the endoscope probe is also limited. Miniature microscope objectives used in conventional fiber bundle microendoscope systems typically consist of optical refractive lenses [16–18] [Fig. 1(a)], gradient refractive index (GRIN) lenses [19–21] [Fig. 1(b)], or other hybrid microlenses [22]. Unfortunately, due to the limitations of sophisticated fabrication processes (such as polishing, molding, and diamond-turning), conventional optical refractive lenses are usually complex in structure and bulky in volume. In addition, it is quite difficult for optical lenses to realize a complicated phase profile. For example, as shown in Fig. 1(a), the optical plano–convex lens can only eliminate on-axis aberrations, but it is difficult to restrain complex off-axis aberration, resulting in blurred imaging at the exit of the fiber bundle. In addition, its outer diameter is on the order of centimeters, which is obviously unsuitable for endoscopic imaging technology that has strict restrictions on the size and performance of the probe. Compared with the conventional ones, the GRIN lens has a smaller volume on the order of millimeters in diameter and a higher but still distorted imaging quality after passing through the optical fiber bundle, as shown in Fig. 1(b). The optical size of the current GRIN lens can be made smaller to 0.35 mm [23] or even 0.25 mm [24] to realize the miniaturization of the probe, but a more optimized imaging

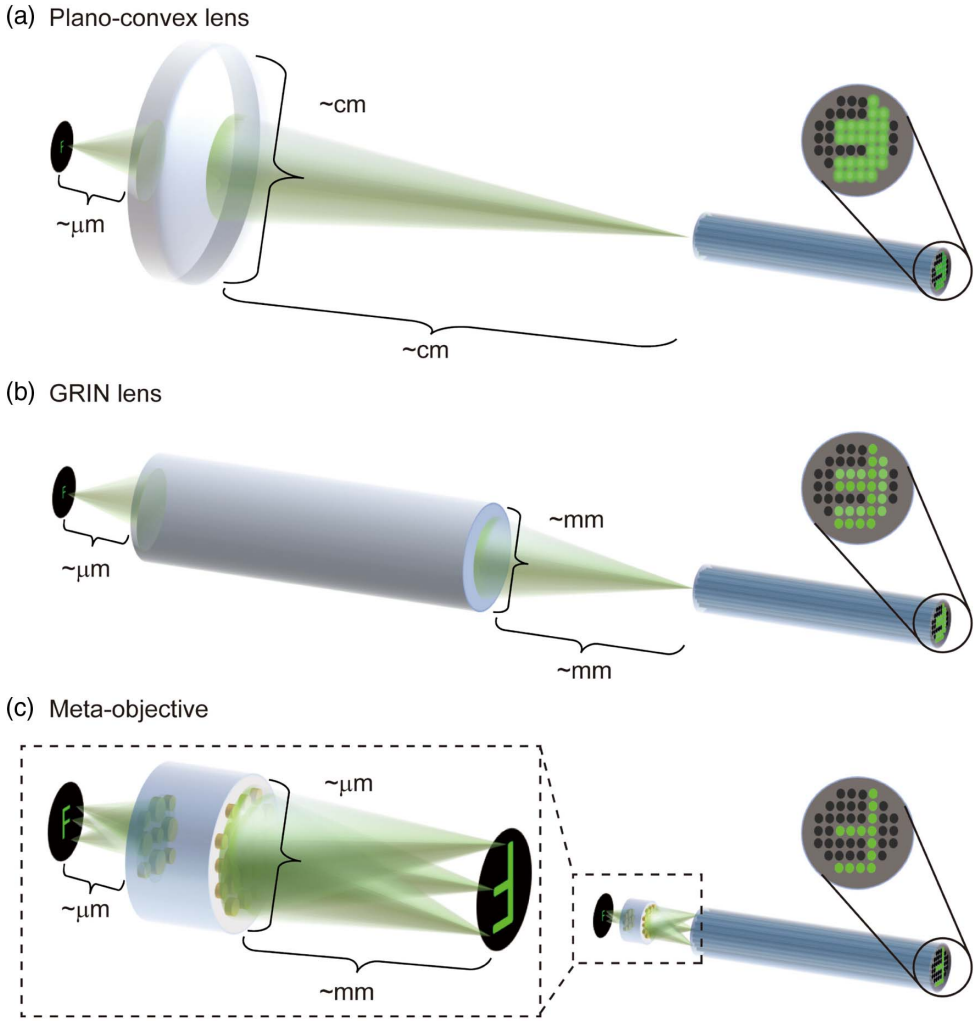

Fig. 1. Schematics of microscope objectives for fiber bundle microendoscopes with different sizes and image qualities. (a) Plano–convex lens-based probe with centimeter diameter. (b) Graded index (GRIN) lens-based probe with millimeter diameter. (c) Probe based on the meta-objective with micrometer diameter, greatly reducing the size of the probe compared with (a) plano–convex lenses and (b) GRIN lenses. The dotted line enlarged section in (c) illustrates that meta-objective can eliminate monochromatic aberrations in full field of view (FOV) of both on- and off-axis, while the plano–convex lens and GRIN lens can only achieve on-axis aberration correction. The solid line magnified parts (rightmost) show the images transmitted through fiber bundles. Obviously, the use of the metalens-based objective produces aberration-free pictures.

performance cannot be simultaneously achieved. Specifically, the off-axis aberration at the edge of the imaging field is extremely difficult to correct. Regardless of various technologies, the microscope objective in most approaches is to pursue the trade-off between miniaturization of the endoscope probes and the imaging performance.

In recent years, along with the rapid development of micro-nano fabrication processing technologies, metalenses, with the ability of manipulating the amplitude, polarization, and phase of an incident beam, exhibit outstanding optical functionalities and have attracted widespread attention [25–29]. Compared with conventional lenses, metalenses are extremely compact and show superior optical performance. A single metalens has been reported to achieve diffraction-limited focusing performance in both near-infrared [30,31] and visible regions [32,33]. Moreover, considerable efforts have been made toward eliminating aberrations of a single metalens. Chromatic aberration is reduced by either the group delay method or the plasmonic resonance method [34–37]. Spherical aberration and astigmatism are eliminated by designing the phase profiles, respectively [38,39]. Third-order Seidel aberrations are corrected by using a front aperture stop that limits the wide beam and a single metalens with optimized phase distribution [40]. However, off-axis aberration cannot be completely corrected through a single metalens, limiting its applications in optical imaging.

Cascaded metalenses can correct the monochromatic aberrations including spherical aberration, comatic aberration, astigmatism, field curvature, and distortion simultaneously [41,42]. Furthermore, they can achieve high-resolution imaging in a large field of view (FOV) [41,42]. Recently, the cascaded metalens has been widely studied and applied to miniaturized optical systems with infinite conjugate imaging [41–46], such as the metalens doublet integrated with a camera

[41], monolithic planar metalens retroreflectors [43], micro-electro-mechanically tunable metalens doublets [44], and spectrometers [45]. On the other hand, there are very few reports on finite conjugate imaging systems, one of which has been proposed in a cascaded metalens for a three-dimensional quantitative phase microscope with micrometer level resolution [47]. Higher resolution is a consistent issue in medical detection and cancer analysis. As shown in Fig. 1(c), the cascaded metalens is used to observe objects at a finite object distance, with the correction of off-axis aberration taken into account in the design process, showing high-resolution imaging quality in a relatively large FOV at the exit of the fiber bundle. At the same time, it can greatly reduce the size of the endoscope probe to several hundred microns. Obviously, the cascaded metalens has great potential to be employed as a miniature microscope objective for the fiber bundle endoscope to achieve high-resolution observation in the limited space of the body cavity.

Here, we comprehensively consider the requirements of fiber bundle endoscopes and propose a meta-objective based on the finite conjugate imaging system of cascaded metalenses. The meta-objective is designed with NA of 0.4, and can correct monochromatic aberrations of 125 μm FOV at the operating wavelength of 525 nm. The meta-objective can achieve 4 times magnification imaging at the designed working distance of 200 μm, and its maximum effective optical diameter is only 400 μm. As shown in Fig. 1(c), the meta-objective is placed in front of the fiber bundle, which can be seen as a simplified fiber bundle microendoscope probe. The proposed meta-objective represents a new direction for the development of high-performance miniaturized fiber bundle endoscopes.

2. RESULTS

A. Design and Fabrication

In order to realize the meta-objective matching the optical fiber bundle endoscopy device, we introduce a miniaturized finite conjugate imaging system based on cascaded metalenses. The working distance and the NA in the object space of the meta-objective are designed as 200 μm and 0.4 respectively, adapting to the penetration depth and sub-micrometer resolution of endoscopic imaging in gastrointestinal tissue. The enlarged section inside the dotted lines in Fig. 1(c) shows a schematic of the meta-objective based on the cascaded metalens, consisting of two metalenses mounted on both sides of a transparent silica film.

As the meta-objective is a finite conjugate imaging system, the aperture stop is placed at the front so that the chief rays in the image space are parallel to the optical axis, ensuring the coupling efficiency of the off-axis rays into the fiber bundle [48]. Generally, optical systems are usually composed of two separate lenses to achieve a large FOV. The front lens has a negative refractive power, catching the strongly refracting chief ray, while the rear group usually has a positive refractive power [48].

We designed two types of optical systems based on a single or cascaded metalens to compare their performances. To reduce the effects of geometric aberrations, the phase profiles of the single metalens and cascaded metalens with NA of 0.4 are optimized over the 125 μm FOV by the ray tracing method (Zemax OpticStudio), as schematically shown in Fig. 2(a). Before optimization, all phase coefficients a_n were set as variables with the initial value of 0. At the same time, it was necessary to define default merit function surface [e.g., root mean square (RMS) spot radius centroid Gaussian quadrature] in the figure of merit listing. The algorithms of orthogonal descent (OD) algorithm and damped least square (DLS) were used for optimization. As a result, the image heights of the single and cascaded metalens on the image plane are 250 μm and 500 μm, respectively, due to their different magnifications. The red, green, and blue rays, respectively, refer to the rays from three radial normalized FOVs: 0.0 Field (F), 0.5 F, and 1.0 F. The three normalized FOVs correspond to on-axis, 62.5 μm FOV, and 125 μm FOV, respectively. For the cascaded metalens case, rays from three FOVs all converge on the same image plane, while the single metalens case exhibits the effect of off-axis aberration, indicating that the cascaded metalens has the ability to eliminate monochromatic aberrations. Comparing the spot diagrams of the single metalens [Fig. 2(b)] and cascaded metalens [Fig. 2(c)], it can be found that the focal spots of the cascaded metalens at 0.5 F and 1.0 F are well limited to the range of the Airy disk, but the single metalens only shows near diffraction limit property in the central FOV, demonstrating that the single metalens cannot eliminate off-axis aberrations. Although only three fields have been drawn in the spot diagrams, it is enough to demonstrate that cascaded metalenses have diffraction-limited performance with negligible monochromatic aberrations on full field, as the RMS spot sizes of each field are within the radius of the diffraction-limited Airy disks. Under off-axis incidences, the cascaded metalens can correct the aberrations, which is hard for the single metalens. The superiority of this performance can be more intuitively displayed through imaging.

As a result, we employed the cascaded metalens case as the meta-objective to achieve macro-magnification imaging at the incident wavelength of 525 nm. In our case, the incident light from the object at 200 μm distance passes through metalens I (operates as the stop aperture and a transmissive negative lens) and then metalens II (acts as a transmissive positive lens) separated by a 500-μm-thick fused silica substrate. The phase profiles of metalens I and metalens II were modeled as cylindrical coordinate radially symmetric polynomials (Binary 2) [42] of the radial coordinate ρ as

$$\varphi(\rho) = \sum_{n=1}^{5} a_n \left(\frac{\rho}{R}\right)^{2n}, \tag{1}$$

where R is the radius of the metalens and a_n is the optimized coefficients. By optimizing the focal spot with the ray tracing technique, the phase profiles of the two metalenses were obtained. The calculated depth of focus (DOF) of the cascaded metalens is 118 μm on-axis for the image plane, as shown in Fig. 2(d).

To implement the two transmissive metalenses, we use a meta-atom to express the subwavelength structure as shown schematically in Fig. 2(e). The meta-atoms consist of nanoposts with a square cross section, depositing on a fused silica substrate. Silicon nitride was selected as the dielectric material of nanoposts, because its refractive index for 525 nm

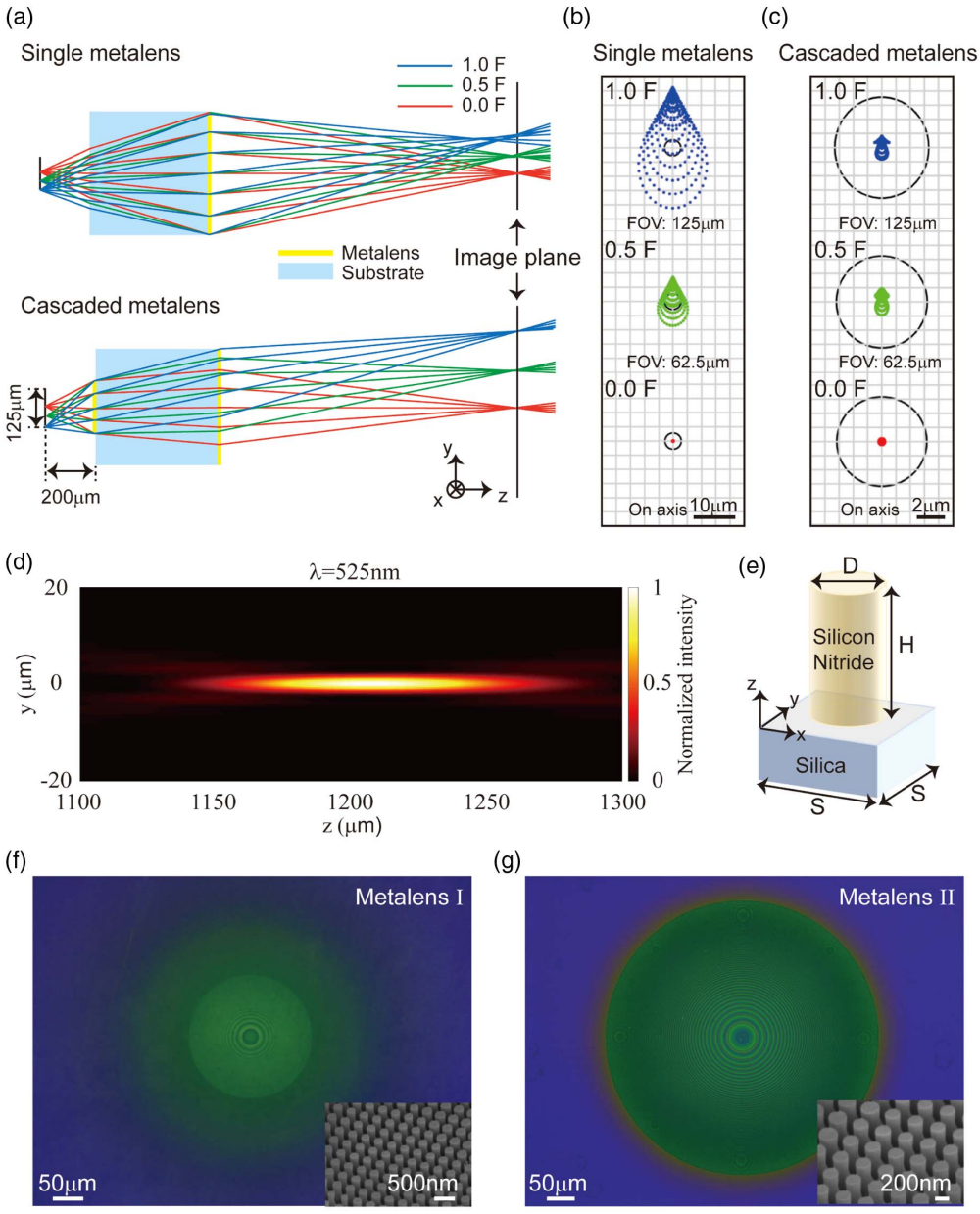

Fig. 2. Ray optics design and sample of the meta-objective without monochromatic aberration. (a) Ray tracing simulation results of the single (top) and cascaded metalens (bottom) of 125 μm FOV at the working distance of 200 μm. The image heights of the single and cascaded metalens on the image plane are about 125 μm and 250 μm, respectively, due to their different magnifications. The blue/green/red rays (referring, respectively, to three normalized FOVs, 0.0 F, 0.5 F, and 1.0 F) have three crossing points at the same image plane in the cascaded case, compared to that of the single case. The three normalized FOVs correspond to on-axis, 62.5 μm FOV, and 125 μm FOV, respectively. (b), (c) Spot diagrams of three normalized FOVs for the two metalenses. The diffuse spot in 1.0 F (blue) is outside/inside the Airy circle (black solid) for the single/cascaded case, respectively. Similar behaviors appear in 0.5 F (green). It indicates that the cascaded metalenses have predominate advantage of eliminating monochromatic aberrations in the full FOV. (d) The calculated normalized intensity distribution of the meta-objective for 0.0 F along the propagation direction in the y-z plane at $\lambda = 525$ nm. Schematic of a meta-atom of the cascaded metalens, consisting of a silicon nitride nanopost on a silica substrate. (e) The nanoposts with the height of 610 nm are arranged in a square lattice with the lattice constant of 380 nm for metalens I, while the corresponding values are 600 and 360 nm for metalens II. The diameters (D) of the nanoposts are variable according to phase distributions. (f), (g) Optical images and side-view SEM images (insets) of the two metalenses.

wavelength is 2 and it has low absorption in the visible spectrum [49]. The height of nanoposts and lattice constant of metalens I were chosen to be 610 nm and 400 nm, respectively. And for metalens II, they were 600 nm and 360 nm, respectively. The nanopost heights and lattice constants of both metalenses are chosen to achieve full 2π phase coverage and have average transmission of 94% [50]. The simulation results of the transmission and phase spectra for y-polarized normal incidence light calculated by rigorous coupled-wave analysis (RCWA) [31,37,49,50] correspond to metalenses I and II,

respectively. It is worth noting that the heights and lattice constants for two metalenses are different due to the different media of the incident and outgoing light at the interface of the two transmissive metalenses.

The fabrication of the cascaded metalens involves fine micro-nano processing technology. Figures 2(f) and 2(g) show the optical images and side-view scanning electron microscope (SEM) images (insets) of the two metalenses. Since the cascaded metalens we designed is a finite conjugate imaging system, the center deviation of the two metalenses on both sides of the same substrate is strictly limited. What is worth mentioning is that the center deviation of the cascaded metalens we prepared is within 1 μm. Compared with the size of the metalens, this deviation introduces very small errors into the optical conjugate system.

B. Characterization

In order to characterize the performance of the meta-objective based on the cascaded metalens, we experimentally measured the focal spots in different FOVs. In the experiment, we used the objective lens to focus the normally incident collimated beam from a tunable continuous wave laser and employed the focal spot as the incidence point source for tests.

Figure 3(a) shows the simulated and measured focal spots intensity profiles of 0.0 F, 0.5 F, and 1.0 F at the incidence with a center wavelength of 525 nm and a bandwidth of 5 nm. The measured focal spot is 4 times magnified relative to the incidence point source. The related x direction cross sections are shown on the right in Fig. 3. The measurement result (blue point) is close to the simulation result (green point). The focal spots in 0.5 F and 1.0 F are similar to the size of the focal spot in 0.0 F, indicating that the meta-objective has the same performance both on and off axis. Fitting the measured focal plane horizontal intensity distributions with the diffraction-limited Airy disk (solid red line), the calculated full widths at half-maximum (FWHMs) are 3.30 μm for 0.0 F, 3.41 μm for 0.5 F, and 3.62 μm for 1.0 F. MTF curves calculated by taking the Fourier transform of the measured focal plane horizontal and vertical intensity distributions from the measurement are displayed in Fig. 3(b). The MTF curves at different fields are close to the diffraction limit (black dashed line), illustrating the excellent monochromatic aberration correction performance of the meta-objective. The MTF curve of 1.0 F along the y direction is slightly deviated. The measured focusing efficiencies of the cascaded metalens are only about 21.6%, 21.5%, and 18.8% for 0.0 F, 0.5 F, and 1.0 F respectively, while the simulated focusing efficiencies are 38.2%, 37.0%, and 35.5%. The measured focusing efficiencies are lower than those obtained in the simulation. That is because of the reflection and scattering caused by excessive oblique incident rays on the rough and non-vertical sidewall of the nanoposts, internal reflection between two metalenses, and the air/substrate interface, and inevitable measurement errors [41].

The resolution of the meta-objective was measured by imaging the negative 1951 USAF target. The light source is from a mercury lamp through bandpass filters with a central wavelength of 525 nm (15 nm bandwidth) and other wavelengths (10 nm bandwidth). As shown in Fig. 3(c) in the middle, element 1 in group 9 (0.977 μm linewidth and gap) and element 3 in group 9 (0.775 μm linewidth and gap) both have more than 20% contrast measurement, indicating that the meta-objective has a sub-micrometer resolution at the designed wavelength of 525 nm. As a finite distance optical imaging system with an NA of 0.4 at 525 nm, the corresponding resolution limit (Rayleigh criterion) of the meta-objective is 0.8 μm. The measurement result is also close to the theoretical limit. In addition to 525 nm, USAF imaging tests were also performed at other wavelengths of visible light. As shown in Fig. 3(c), in the range of 430 nm to 680 nm (the bandpass filters with bandwidth of 10 nm), the resolution of the meta-objective is approximately 775 nm. The imaging contrast results of element 3 in group 9 show that the near diffraction limit image can be obtained not only at the designed wavelength of 525 nm, but also in several other visible regions. It should be pointed out that in order to obtain the images with a magnification of 4, we imaged the USAF resolution target at different wavelengths at different object distances.

In order to measure the magnification ability of the meta-objective, we designed and fabricated the object (letter "F") with the height of 100 μm for imaging. According to the test results, 4 times magnification imaging was achieved, meeting the design requirements. Further, images of different magnification rates can also be obtained by changing object distance. As shown in Fig. 4(a), in the range of 430 nm to 680 nm, 4 times magnification "F" images can be obtained at certain object distances. In addition, as shown in Fig. 4(b), imaging with different magnification rates can be obtained at different object distances. The magnification decreases gradually as the object distance increases. The insets in Fig. 4(b) are images of different magnifications of "F" obtained in experiments, noting that their scale bars are different. And the magnification rates obtained by the experiment (blue hollow circles) are in perfect agreement with the curve obtained by simulation (red solid line). This flexible magnification characteristic reduces the strict constrains on the working distance in application. All magnified images are clear and undistorted. This is due to the design of the meta-objective to eliminate monochromatic aberrations.

To compare the imaging performance of the meta-objective and other optical lenses, the water lily slice and the *Bacillus cereus* were also observed. Here we employed the plano–convex lens (Thorlabs, LA1805-A) and a GRIN lens (GoFoton, ILW-200-ZSU01) to image the same area for contrast. As shown in Fig. 4(c), when observing the water lily slice, an image with clearer texture of the cell walls (yellow dotted boxes) of the mesophyll tissue can be acquired by using a meta-objective than with other optical lenses. The plant slice has a certain thickness, and we can obtain more depth information by observing with the meta-objective. Furthermore, when observing *Bacillus cereus*, more details can be gathered by using the meta-objective. It is obvious that there are no large numbers of bacterial groups in the two positions indicated by the white and red dotted boxes. This situation is not so apparent for the GRIN lens and completely indistinguishable for the plano–convex lens. The visualizations of the cell walls of water lily and the clear delineation of *Bacillus cereus* with rod shape in countless colonies further emphasize the superior imaging quality of the meta-objective over other conventional optical elements.

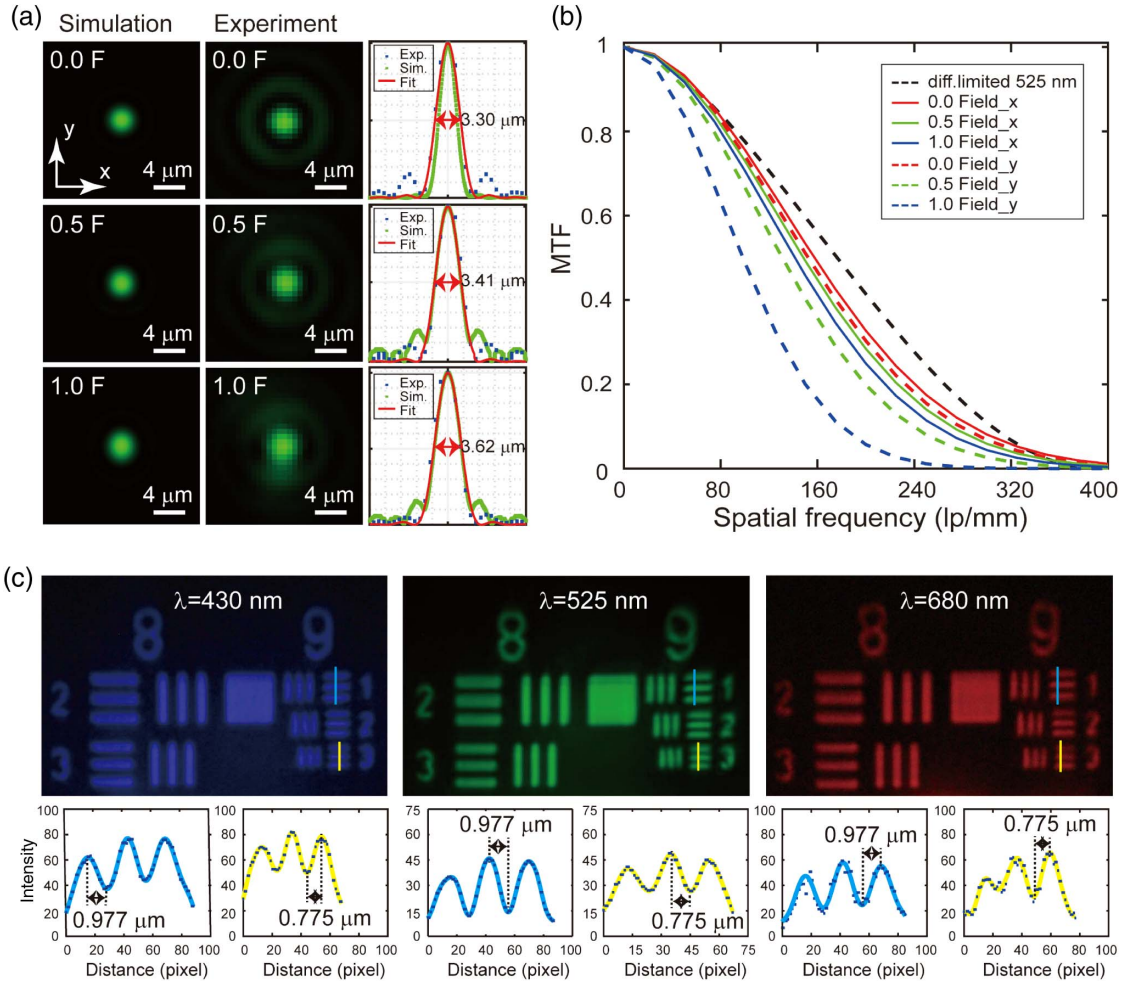

Fig. 3. Near diffraction limit sub-micrometer resolution characterization of the meta-objective at different incident wavelengths. (a) Simulated and measured focal spot diagrams and focal spot intensity profiles in 0.0 F, 0.5 F, 1.0 F of the meta-objective at 525 nm wavelength. The measured focal spot is 4 times magnified relative to the incidence point source. The experimental results of focal spots are in good agreement with their simulation results. The focal spots in 0.5 F and 1.0 F are similar to the focal spot in 0.0 F in size, indicating the performance of the meta-objective to eliminate monochromatic aberration. Fitting with Airy function, the full widths at half-maximum (FWHMs) of the measured focal spots along the x direction are 3.30 μm for 0.0 F, 3.41 μm for 0.5 F, and 3.62 μm for 1.0 F. (b) Corresponding to (a), the MTF curves in 0.0 F, 0.5 F, 1.0 F obtained by experiments. MTF curves in three fields of view are close to the MTF curve of the diffraction limit (black dotted line), further illustrating the high-resolution performance of the meta-objective. (c) Resolution tests by imaging a negative 1951 United States Air Force (USAF) target at wavelengths of 430 nm, 525 nm, and 680 nm. For 525 nm, the element 3 in group 9 (645 lp/mm, 0.775 μm linewidth, yellow line) and element 1 in group 9 (512 lp/mm, 0.977 μm linewidth, blue line) both have a contrast ratio of more than 20%, indicating that the meta-objective can resolve sub-micrometer details. Similar properties are also shown for 430 nm, 680 nm, and other more incident wavelengths.

C. Imaging with Fiber Bundle Microendoscope

We applied the meta-objective to the fiber bundle microscope imaging system to explore the possibility of using it as an endoscope objective. To demonstrate the imaging quality of the meta-objective, we compared it with several other conventional optical elements including a plano–convex lens and a GRIN lens by using the measurement setup shown in Fig. 5(a). The incoherent light from a white light source device (Thorlabs, OSL2) passed through a pinhole and a bandpass filter with 525 nm central wavelengths (Edmund, bandpass filter, bandwidth 15 nm) in turn before illuminating the test object. The resolution test was performed using the 1951 USAF target (Edmund, Hi-Resolution Negative Target). Through the meta-objective, a plano–convex lens (Thorlabs, LA1805-A), or a GRIN lens (GoFoton, ILW-200-ZSU01), the object can form equal or magnified images. A customized 30-cm-long fiber bundle of more than 3900 fiber cores with a core diameter of 8 μm was placed before a 10× objective (Olympus, MPLFLN10xBD), a tube lens (Thorlabs, ITL200), and a color charge-coupled device (CCD) camera (Mshot, MC20), which formed a fiber bundle microendoscope imaging system.

The combination with the fiber bundle and meta-objective or the conventional optical elements can be regarded as a primitive fiber bundle microendoscope probe. After imaging with the probes, pixelated original pictures are obtained. Since the most prominent feature in all original images is the honeycomb structures, Gaussian filter and edge detection algorithm are applied to all raw images [4,21]. The lensless fiber bundle probe is

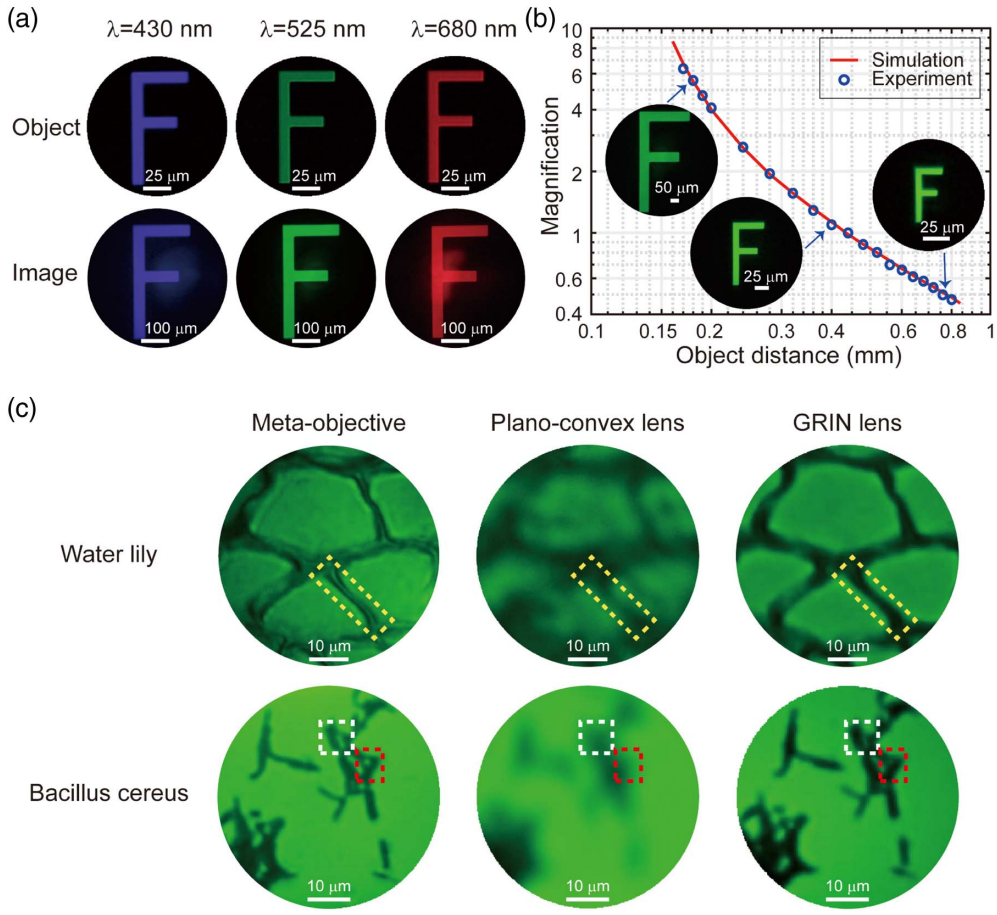

Fig. 4. Different magnification imaging and biological imaging tests of the meta-objective. (a) Four times magnification imaging of letter "F" at wavelengths of 430 nm, 525 nm, and 680 nm. (b) The magnification graph of the meta-objective as a function of object distance. The experimental results (blue hollow circles) agree well with the simulation curve (red solid line). The insets are the corresponding images of letter "F" obtained in the experiment with different scale bars. (c) Imaging of water lily leaf slice and *Bacillus cereus* slice with the meta-objective, plano–convex lens, and GRIN lens, respectively. The yellow dotted boxes represent the cell wall of the water lily leaf's mesophyll tissue. More depth information about the cell wall was obtained with the meta-objective, while only the outline could be distinguished with a GRIN lens, and the more blurred image was acquired with the plano–convex lens. The white and red dotted boxes indicate the gaps between the communities of *Bacillus cereus*. Similarly, the tiny spacing between bacterial groups can be identified with meta-objective, not obvious enough with a GRIN lens, and totally indistinguishable with a plano–convex lens.

only capable of 12.41 μm resolution (element 3 in group 5). In Fig. 5(b), the transverse resolutions of the microscope imaging system using different fiber bundle probes with the meta-objective, plano–convex lens, or GRIN lens are 2.19 μm (element 6 in group 7), 8.77 μm (element 6 in group 5), and 4.39 μm (element 6 in group 6), respectively. It can be seen that the meta-objective-based fiber bundle probe shows better imaging performance than others.

In addition, we demonstrated the biological slice of water lily by using the fiber bundle probe based on the meta-objective and other conventional lens-based fiber bundle probes as shown in Fig. 5(c). Images were processed to increase the visibility. We used the fiber bundle microendoscope imaging system to observe the cells in the area (red circle) near the palisade tissue. Clearer images of a greater magnification can be obtained with a lens placed in front of the fiber bundle in experiment. In contrast to the images formed by using a plano–convex lens or GRIN lens, the image with a higher resolution can be achieved by using the meta-objective. In Fig. 5(c), the outlines of the mesophyll cells (orange arrows) are more obvious, and the spacing between their cell walls (white arrows) is better to be distinguished with the probe based on the meta-objective, proving that it has superior performance over other conventional optical probes as mentioned above. In our case, the lateral resolution of the fiber bundle microendoscope is limited by the fiber bundle, not the meta-objective we designed.

3. DISCUSSION

High resolution and miniaturization have always been the focus of research on the fiber bundle microendoscope. In terms of resolution, the meta-objective we designed has sub-micrometer resolution. Compared with a plano–convex lens and a miniaturized GRIN lens, higher quality images can be achieved with the meta-objective when observing plant and bacterial slices. However, although the resolution of the fiber bundle probe

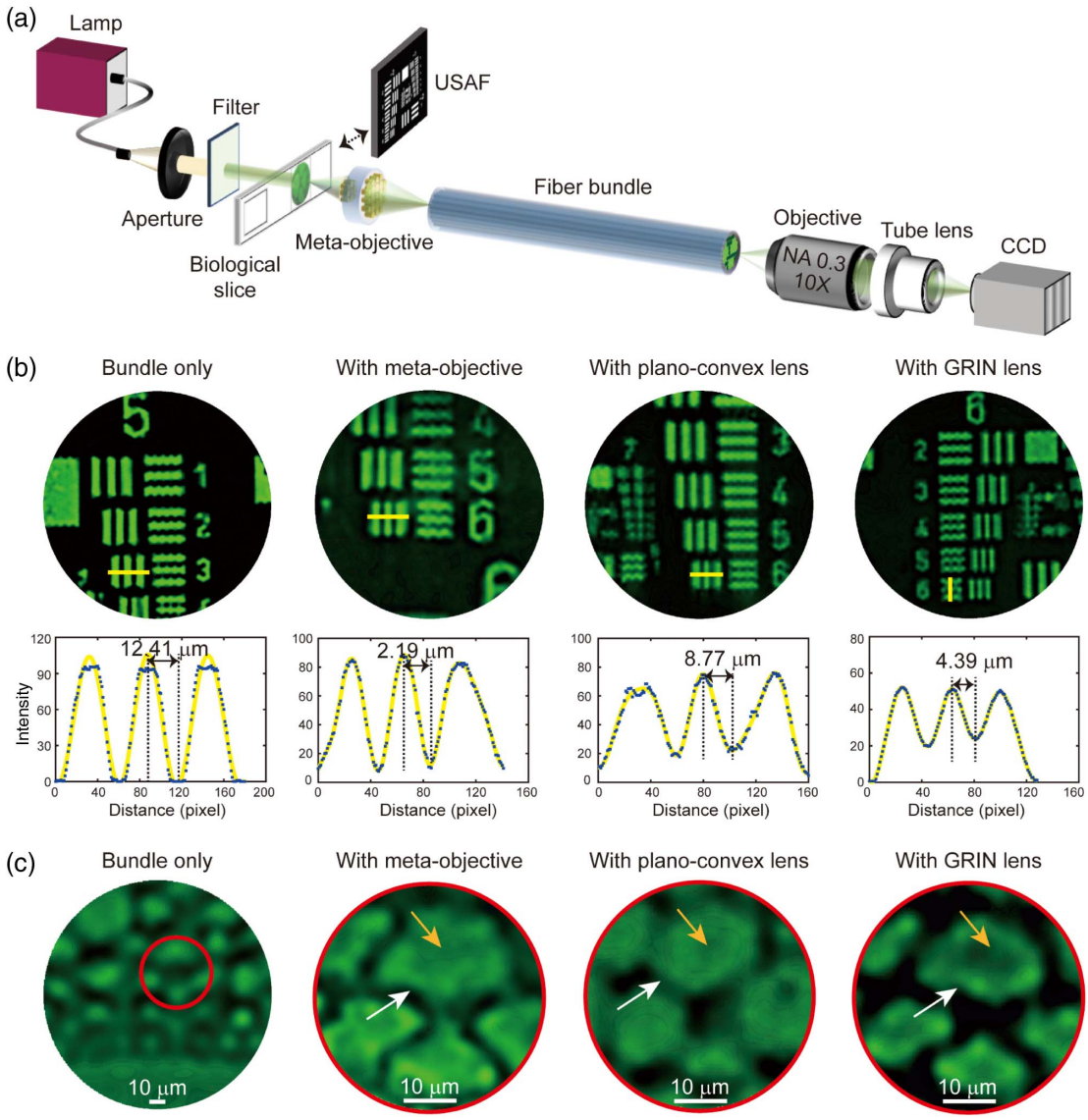

Fig. 5. Fiber bundle microendoscope with a meta-objective. (a) Schematic of the measurement setup. A customized 30-cm-long fiber bundle of more than 3900 fiber cores with a core diameter of 8 μm was employed here, combined with optical lenses for use as the probes of fiber bundle microendoscopes. (b) Resolution tests by imaging a negative 1951 USAF target using the fiber bundle microscope imaging system. The resolvable linewidths are 2.19 μm (element 6 in group 7, 228 lp/mm) with the meta-objective, 8.77 μm (element 6 in group 5, 57 lp/mm) with the plano–convex lens, and 4.39 μm (element 6 in group 6, 114 lp/mm) with the GRIN lens. The intrinsic resolution of the system without a lens is 12.41 μm (elements 3 in group 5, 40 lp/mm), provided as a reference. (c) Imaging of biological slice (water lily). Compared with the image directly transmitted through the fiber bundle only, the resolution is improved after introducing optical lenses as objectives placed in front of the fiber bundle. The orange arrows and the white arrows indicate the mesophyll cells and the cell wall, respectively. A more realistic image can be obtained with the meta-objective, while the image acquired with a GRIN lens will be distorted and even worse with the plano–convex lens. The displayed pictures in (b) and (c) are processed with the image post-processing technique to improve visualization.

based on the meta-objective has been improved dramatically, it is still limited by the monofilament diameter and core spacing of the fiber bundle, which is difficult to reduce below 1 μm. The monofilament diameter of the fiber bundle we used here is only 8 μm. If a fiber bundle with a smaller monofilament diameter is employed, the imaging quality of the microendoscope will be further improved. At present, the FOV of the meta-objective we designed is still not large enough. That is because the FOV and resolution of meta-objective are mutually restricted in the design principle and it is difficult to further increase the FOV while ensuring the high resolution of the meta-objective. In addition, the proposed meta-objective only eliminates monochromatic aberration, but not chromatic aberration. If possible, we can realize broadband functionality by designing nanoposts with a wider equivalent refractive index to form the meta-objective.

For flat optics, we should note that many functions of the above mentioned metalenses could be realized equally well by conventional multilevel diffractive lenses (MDLs) [51,52]. As a new technology in the last two decades, metalenses have more

degrees of freedom than MDLs [52], for example, high-NA capability with high efficiency [31,33], polarization selectivity [52], tunability [53], and some other unexplored advantages in terms of future metalens applications. However, we also suggest that the metalenses do not replace MDLs since MDLs have their own advantages, for example, cost effectiveness and simplicity to manufacture. In this paper, the meta-objective designed by us is fixed and insensitive to polarization. Although it has not brought the unique advantages of metalenses into full play yet, it cannot hinder the efforts of metalenses in imaging applications. We believe such metalenses could be mass fabricated in the foundry of complementary metal oxide semiconductor (CMOS)-compatible semiconductor manufacturers in the near future.

When it comes to miniaturization and integration, the meta-objective with the effective optical diameter of only 400 μm can match the fiber bundle with the diameter of 500 μm, and there is a certain air gap between them. Unique flat properties of the meta-objective can ease the tight tolerance requirement for both optical and mechanical components, dramatically reducing the time for assembly [48]. Moreover, considering the processing of the connector and the cutting process of the substrate, it is not difficult to prepare a hundred micron-level fiber bundle endoscope probe.

In conclusion, we have developed a meta-objective based on cascaded metalenses, acting as a miniature microscope objective at the distal end of a fiber bundle. We experimentally demonstrated that the meta-objective within 0.5 mm^3 volume has the ability to achieve near diffraction-limited resolution imaging over 125 μm FOV. According to the proposed capabilities, the fiber bundle microendoscope based on the meta-objective has superior resolution and miniaturization of structure, and works intrinsically with incoherent illumination in a single shot without scanning. In the present study, although we only demonstrated the performance of the meta-objective combined with a fiber bundle without pasting them, there is no essential limitation on the development of the miniature endoscope probe based on the meta-objective.

Arising from minimally invasive and superior resolution biological imaging in the application of the meta-objective to fiber bundle microendoscope, we believe that the most promising benefit is the possibility of combination with the fluorescence confocal microscopy. In addition, we aim to overcome limitations and enhance the performances of the endoscope for portable minimally invasive detection and surgery, depending on fundamental properties of metalenses and advanced nanofabrication techniques. Overall, the presented meta-objective indicates an alternative design to ultrathin micro-optical elements with great potential for biomedical applications. Although further work is needed to develop the optimal approach for *in vivo* imaging and even clinical application, it could provide a more effective alternative to microminiaturization of bio-optical devices.

Funding. National Natural Science Foundation of China (62035016, 61775243, 61805288, 61905291); National Key Research and Development Program of China (2019YFB2203502); Guangdong Basic and Applied Basic Research Foundation (2018B030308005, 2020A1515010626); Guangzhou Science, Technology and Innovation Commission (201804020029); Fundamental Research Funds for the Central Universities.

Disclosures. The authors declare no conflicts of interest.

†These authors contributed equally to this work.

REFERENCES

1. R. A. Natalin and J. Landman, "Where next for the endoscope?" Nat. Rev. Urol. **6**, 622–628 (2009).
2. D. Ramai, K. Zakhia, D. Etienne, and M. Reddy, "Philipp Bozzini (1773–1809): the earliest description of endoscopy," J. Med. Biography **26**, 137–141 (2018).
3. M. Hughes, T. P. Chang, and G.-Z. Yang, "Fiber bundle endocytoscopy," Biomed. Opt. Express **4**, 2781–2794 (2013).
4. M. Kim, J. Hong, J. Kim, and H.-J. Shin, "Fiber bundle-based integrated platform for wide-field fluorescence imaging and patterned optical stimulation for modulation of vasoconstriction in the deep brain of a living animal," Biomed. Opt. Express **8**, 2781–2795 (2017).
5. P. Kim, E. Chung, H. Yamashita, K. E. Hung, A. Mizoguchi, R. Kucherlapati, D. Fukumura, R. K. Jain, and S. H. Yun, "*In vivo* wide-area cellular imaging by side-view endomicroscopy," Nat. Methods **7**, 303–305 (2010).
6. Y.-H. Seo, K. Hwang, and K.-H. Jeong, "1.65 mm diameter forward-viewing confocal endomicroscopic catheter using a flip-chip bonded electrothermal MEMS fiber scanner," Opt. Express **26**, 4780–4785 (2018).
7. M. E. Bocarsly, W.-C. Jiang, C. Wang, J. T. Dudman, N. Ji, and Y. Aponte, "Minimally invasive microendoscopy system for *in vivo* functional imaging of deep nuclei in the mouse brain," Biomed. Opt. Express **6**, 4546–4556 (2015).
8. D. Reismann, J. Stefanowski, R. Günther, A. Rakhymzhan, R. Matthys, R. Nützi, S. Zehentmeier, K. Schmidt-Bleek, G. Petkau, H.-D. Chang, S. Naundorf, Y. Winter, F. Melchers, G. Duda, A. E. Hauser, and R. A. Niesner, "Longitudinal intravital imaging of the femoral bone marrow reveals plasticity within marrow vasculature," Nat. Commun. **8**, 2153 (2017).
9. T. A. Murray and M. J. Levene, "Singlet gradient index lens for deep *in vivo* multiphoton microscopy," J. Biomed. Opt. **17**, 021106 (2012).
10. J. H. Jennings, C. K. Kim, J. H. Marshel, M. Raffiee, L. Ye, S. Quirin, S. Pak, C. Ramakrishnan, and K. Deisseroth, "Interacting neural ensembles in orbitofrontal cortex for social and feeding behaviour," Nature **565**, 645–649 (2019).
11. M. A. A. Neil, R. Juškaitis, and T. Wilson, "Method of obtaining optical sectioning by using structured light in a conventional microscope," Opt. Lett. **22**, 1905–1907 (1997).
12. T. S. Tkaczyk, M. Rahman, V. Mack, K. Sokolov, J. D. Rogers, R. Richards-Kortum, and M. R. Descour, "High resolution, molecular-specific, reflectance imaging in optically dense tissue phantoms with structured-illumination," Opt. Express **12**, 3745–3758 (2004).
13. H. Neumann, M. Vieth, M. F. Neurath, and F. S. Fuchs, "*In vivo* diagnosis of small-cell lung cancer by endocytoscopy," J. Clin. Oncol. **29**, e131–e132 (2011).
14. T. Arao, K. Yanagihara, M. Takigahira, M. Takeda, F. Koizumi, Y. Shiratori, and K. Nishio, "ZD6474 inhibits tumor growth and intraperitoneal dissemination in a highly metastatic orthotopic gastric cancer model," Int. J. Cancer **118**, 483–489 (2006).
15. S. Saha, A. Bardelli, P. Buckhaults, V. E. Velculescu, C. Rago, B. S. Croix, K. E. Romans, M. A. Choti, C. Lengauer, K. W. Kinzler, and B. Vogelstein, "A phosphatase associated with metastasis of colorectal cancer," Science **294**, 1343–1346 (2001).
16. C. Liang, K.-B. Sung, R. R. Richards-Kortum, and M. R. Descour, "Design of a high-numerical-aperture miniature microscope objective for an endoscopic fiber confocal reflectance microscope," Appl. Opt. **41**, 4603–4610 (2002).

17. L. Yang, J. Wang, G. Tian, J. Yuan, Q. Liu, and L. Fu, "Five-lens, easy-to-implement miniature objective for a fluorescence confocal microendoscope," Opt. Express **24**, 473–484 (2016).
18. J. Wang, H. Li, G. Tian, Y. Deng, Q. Liu, and L. Fu, "Near-infrared probe-based confocal microendoscope for deep-tissue imaging," Biomed. Opt. Express **9**, 5011–5025 (2018).
19. J. Knittel, L. Schnieder, G. Buess, B. Messerschmidt, and T. Possner, "Endoscope-compatible confocal microscope using a gradient index-lens system," Opt. Commun. **188**, 267–273 (2001).
20. W. Göbel, J. N. D. Kerr, A. Nimmerjahn, and F. Helmchen, "Miniaturized two-photon microscope based on a flexible coherent fiber bundle and a gradient-index lens objective," Opt. Lett. **29**, 2521–2523 (2004).
21. Y. Chang, W. Lin, J. Cheng, and S. C. Chen, "Compact high-resolution endomicroscopy based on fiber bundles and image stitching," Opt. Lett. **43**, 4168–4171 (2018).
22. B. A. Flusberg, A. Nimmerjahn, E. D. Cocker, E. A. Mukamel, R. P. J. Barretto, T. H. Ko, L. D. Burns, J. C. Jung, and M. J. Schnitzer, "High-speed, miniaturized fluorescence microscopy in freely moving mice," Nat. Methods **5**, 935–938 (2008).
23. M. J. Levene, D. A. Dombeck, K. A. Kasischke, R. P. Molloy, and W. W. Webb, "*In vivo* multiphoton microscopy of deep brain tissue," J. Neurophysiol. **91**, 1908–1912 (2004).
24. X. Li, C. Chudoba, T. Ko, C. Pitris, and J. G. Fujimoto, "Imaging needle for optical coherence tomography," Opt. Lett. **25**, 1520–1522 (2000).
25. S. M. Kamali, E. Arbabi, A. Arbabi, and A. Faraon, "A review of dielectric optical metasurfaces for wavefront control," Nanophotonics **7**, 1041–1068 (2018).
26. M. L. Tseng, H.-H. Hsiao, C. H. Chu, M. K. Chen, G. Sun, A.-Q. Liu, and D. P. Tsai, "Metalenses: advances and applications," Adv. Opt. Mater. **6**, 1800554 (2018).
27. B. Li, W. Piyawattanametha, and Z. Qiu, "Metalens-based miniaturized optical systems," Micromachines **10**, 310 (2019).
28. S. Sun, Q. He, J. Hao, S. Xiao, and L. Zhou, "Electromagnetic metasurfaces: physics and applications," Adv. Opt. Photon. **11**, 380–479 (2019).
29. X. Zou, G. Zheng, Q. Yuan, W. Zang, R. Chen, T. Li, L. Li, S. Wang, Z. Wang, and S. Zhu, "Imaging based on metalenses," PhotoniX **1**, 2 (2020).
30. A. Arbabi, Y. Horie, M. Bagheri, and A. Faraon, "Dielectric metasurfaces for complete control of phase and polarization with subwavelength spatial resolution and high transmission," Nat. Nanotechnol. **10**, 937–943 (2015).
31. A. Arbabi, Y. Horie, A. J. Ball, M. Bagheri, and A. Faraon, "Subwavelength-thick lenses with high numerical apertures and large efficiency based on high-contrast transmitarrays," Nat. Commun. **6**, 7069 (2015).
32. X. Ni, S. Ishii, A. V. Kildishev, and V. M. Shalaev, "Ultra-thin, planar, Babinet-inverted plasmonic metalenses," Light Sci. Appl. **2**, e72 (2013).
33. M. Khorasaninejad, W. T. Chen, R. C. Devlin, J. Oh, A. Y. Zhu, and F. Capasso, "Metalenses at visible wavelengths: diffraction-limited focusing and subwavelength resolution imaging," Science **352**, 1190–1194 (2016).
34. E. Arbabi, A. Arbabi, S. M. Kamali, Y. Horie, and A. Faraon, "Controlling the sign of chromatic dispersion in diffractive optics with dielectric metasurfaces," Optica **4**, 625–632 (2017).
35. S. Wang, P. C. Wu, V.-C. Su, Y.-C. Lai, C. Hung Chu, J.-W. Chen, S.-H. Lu, J. Chen, B. Xu, C.-H. Kuan, T. Li, S. Zhu, and D. P. Tsai, "Broadband achromatic optical metasurface devices," Nat. Commun. **8**, 187 (2017).
36. W. T. Chen, A. Y. Zhu, V. Sanjeev, M. Khorasaninejad, Z. Shi, E. Lee, and F. Capasso, "A broadband achromatic metalens for focusing and imaging in the visible," Nat. Nanotechnol. **13**, 220–226 (2018).
37. Z.-B. Fan, H.-Y. Qiu, H.-L. Zhang, X.-N. Pang, L.-D. Zhou, L. Liu, H. Ren, Q.-H. Wang, and J.-W. Dong, "A broadband achromatic metalens array for integral imaging in the visible," Light Sci. Appl. **8**, 67 (2019).
38. H. Pahlevaninezhad, M. Khorasaninejad, Y.-W. Huang, Z. Shi, L. P. Hariri, D. C. Adams, V. Ding, A. Zhu, C.-W. Qiu, F. Capasso, and M. J. Suter, "Nano-optic endoscope for high-resolution optical coherence tomography in vivo," Nat. Photonics **12**, 540–547 (2018).
39. C. Chen, W. Song, J.-W. Chen, J.-H. Wang, Y. H. Chen, B. Xu, M.-K. Chen, H. Li, B. Fang, J. Chen, H. Y. Kuo, S. Wang, D. P. Tsai, S. Zhu, and T. Li, "Spectral tomographic imaging with aplanatic metalens," Light Sci. Appl. **8**, 99 (2019).
40. M. Y. Shalaginov, S. An, F. Yang, P. Su, D. Lyzwa, A. M. Agarwal, H. Zhang, J. Hu, and T. Gu, "Single-element diffraction-limited fisheye metalens," Nano Lett. **20**, 7429–7437 (2020).
41. A. Arbabi, E. Arbabi, S. M. Kamali, Y. Horie, S. Han, and A. Faraon, "Miniature optical planar camera based on a wide-angle metasurface doublet corrected for monochromatic aberrations," Nat. Commun. **7**, 13682 (2016).
42. B. Groever, W. T. Chen, and F. Capasso, "Meta-lens doublet in the visible region," Nano Lett. **17**, 4902–4907 (2017).
43. A. Arbabi, E. Arbabi, Y. Horie, S. M. Kamali, and A. Faraon, "Planar metasurface retroreflector," Nat. Photonics **11**, 415–420 (2017).
44. E. Arbabi, A. Arbabi, S. M. Kamali, Y. Horie, M. Faraji-Dana, and A. Faraon, "MEMS-tunable dielectric metasurface lens," Nat. Commun. **9**, 812 (2018).
45. M. Faraji-Dana, E. Arbabi, A. Arbabi, S. M. Kamali, H. Kwon, and A. Faraon, "Compact folded metasurface spectrometer," Nat. Commun. **9**, 4196 (2018).
46. M. Faraji-Dana, E. Arbabi, H. Kwon, S. M. Kamali, A. Arbabi, J. G. Bartholomew, and A. Faraon, "Hyperspectral imager with folded metasurface optics," ACS Photon. **6**, 2161–2167 (2019).
47. H. Kwon, E. Arbabi, S. M. Kamali, M. Faraji-Dana, and A. Faraon, "Single-shot quantitative phase gradient microscopy using a system of multifunctional metasurfaces," Nat. Photonics **14**, 109–114 (2020).
48. R. Liang, "Endoscope Optics," in *Optical Design for Biomedical Imaging* (SPIE, 2011), pp. 399–410.
49. Z.-B. Fan, Z.-K. Shao, M.-Y. Xie, X.-N. Pang, W.-S. Ruan, F.-L. Zhao, Y.-J. Chen, S.-Y. Yu, and J.-W. Dong, "Silicon nitride metalenses for close-to-one numerical aperture and wide-angle visible imaging," Phys. Rev. Appl. **10**, 014005 (2018).
50. V. Liu and S. Fan, "S4: a free electromagnetic solver for layered periodic structures," Comput. Phys. Commun. **183**, 2233–2244 (2012).
51. S. Banerji, M. Meem, A. Majumder, F. G. Vasquez, B. Sensale-Rodriguez, and R. Menon, "Imaging with flat optics: metalenses or diffractive lenses?" Optica **6**, 805–810 (2019).
52. J. Engelberg and U. Levy, "The advantages of metalenses over diffractive lenses," Nat. Commun. **11**, 1991 (2020).
53. P. P. Iyer, R. A. DeCrescent, T. Lewi, N. Antonellis, and J. A. Schuller, "Uniform thermo-optic tunability of dielectric metalenses," Phys. Rev. Appl. **10**, 044029 (2018).